Metamaterial-Based Electronic Skin with Conformality and Multisensory Integration

Nan Li, Liwu Liu,* Yanju Liu,* and Jinsong Leng

Mechanical metamaterials (MMs) receive widespread attention due to their unprecedented mechanical properties. However, in the next-generation MMs, the cognitive function of information processing can be realized while maintaining superior mechanical properties. Herein, a mechanical metamaterial-based self-powered electronic skin (e-skin) with multimodal fusion perception capability and shape memory reconfigurability is proposed. Benefiting from an MM skeleton and its analytical model, e-skin realizes biomimetic nonlinear mechanical behavior and mechanical reconfigurability to imitate target biotissues. Its integrated perovskite-based elastic sensors enable high-precision collection of physiological movements and auditory, tactile, and precontact distance signals. Further, by imitating the integration and interaction functions in biological multisensory neural networks, the system achieves advanced cognitive functions of acquiring, identifying, and integrating information across modalities. Applications of e-skin are demonstrated in motion monitoring, speech recognition, and somatosensory game operation. These capabilities can be applied to cross-modal perception robot systems based on multisensory neural networks.

1. Introduction

Mechanical Metamaterials (MMs) can achieve superior and unprecedent mechanical properties through rational microstructural designs. In the past few decades, they have exhibited outstanding mechanical advantages in the space industry, aviation industry, tissue engineering, flexible electronics, and other fields. Recent studies have demonstrated that self-sensing and shape memory materials can be used to create intelligent mechanical metamaterials and achieve advanced functions beyond their mechanical properties.[1] This means that MMs can transition to application fields other than mechanical such as sensing,[2–4] energy harvesting,[5] actuation, adaptation,[6] computing,[7] and information processing.[8] For example, humans explore, learn, and adapt to the complex natural world by collecting visual, tactile, auditory, olfactory, and taste signals through multisensory systems and interacting with information through the integration of neural and muscular systems.[9] By integrating to electronic skin (e-skin) that imitates the perception-decision-response cycle of the human nervous system, a new generation of MMs have broad application prospects in revolutionary fields such as the Internet of Things (IoTs) and brain–computer interfaces.[10–12]

Current research on e-skin has mainly focused on improving the sensing performance of the functional components and optimizing the mechanical properties of the system. The former enables superior perception capabilities,[13–15] whereas the latter strives to obtain a flexible structure that is closer to the mechanical properties of soft biological tissues.[16,17] However, e-skins have several limitations. For example, traditional tactile sensing elements only generate signals when physically touched or intruded, and cannot predict the response action to a stimulus before contact.[18,19] Although pre-contact sensors in existing studies can achieve functionality by utilizing optical sensing elements,[20,21] electromagnetic technology,[22] or ultrasonic transducers,[23] they are severely affected by environmental parameters. Moreover, the traditional power supply strategy for e-skin is faced with several drawbacks, including limited life, limited mobility and complexity of the system. The reliance on external power sources can hinder the development of truly lightweight, compact, and user-friendly flexible electronics, which are essential for seamless integration into daily life. Further, with the development of wearable devices[24,25] and flexible electronics,[26–29] there is an urgent need for e-skins with excellent mechanical properties and multimodal sensing functions for the new generation of multimodal information acquisition and fusion perception systems.[30–34]

However, existing research on the mechanical properties of e-skin has mainly focused on reducing Young's modulus of the structure to improve its compliance with the skin,[35–37] while ignoring the other mechanical properties of biological tissues.[38] Therefore, MMs with unprecedent mechanical properties are considered ideal candidates. Their superior mechanical properties usually combine low elastic modulus, high stretchability, high tensile strength[39] and nonlinear mechanical behavior commonly found in biological tissues. For example, MMs with a J-shaped nonlinear mechanical behavior exhibit sufficient

N. Li, L. Liu, Y. Liu
Department of Astronautical Science and Mechanics
Harbin Institute of Technology (HIT)
P.O. Box 301, No. 92 West Dazhi Street, Harbin 150001, P. R. China
E-mail: liulw@hit.edu.cn; yj_liu@hit.edu.cn
J. Leng
Center for Composite Materials and Structures
Harbin Institute of Technology (HIT)
P.O. Box 3011, No. 2 Yikuang Street, Harbin 150080, P. R. China

conformality when wrapping dynamic biological tissues/organs.[40,41] Therefore, MMs have been applied in cutting-edge fields and have attained revolutionary achievements such as MM-based artificial skin,[42] stretchable strain sensors,[43] and metasurface-based invisible skin.[44] However, most of MMs are fabricated with fixed configurations, which means their structures and mechanical properties cannot be adjusted to meet different usage requirements. This limitation restricts the universal adaptability of MM-based e-skin. Recent research indicated that MMs made from shape memory polymers (SMPs) can automatically transform into predesigned shapes under external excitation, providing a new solution to achieve e-skins with adaptive mechanical properties.

Herein, an MM-based self-powered e-skin was proposed with multimodal fusion-perception capabilities and shape memory reconfigurability. It realized the precise acquisition of vibration, deformation, and pre-contact distance signals using perovskite-based elastic sensors. The design of the MM skeleton significantly improved the mechanical imbalance between e-skin and dynamic tissues, which enables the precise transmission of physiological motor information. In addition, the MM skeleton enabled e-skin with the shape reconfiguration function corresponding to certain stimuli to imitate the mechanical properties of biotissues. Further, e-skin achieved self-powering and wireless information interaction for real-time human motor monitoring, sound signals recognition, target orientation, and somatosensory game manipulation. These functions verified the multimodal signal detection function of e-skin in real scenarios. In summary, e-skin not only realized excellent mechanical properties and high conformal deformation ability similar to that of biological skin but also integrated the multimodal signal acquisition function of hearing, touch, and vision of a biomimetic sensory system. It is a promising candidate for application in soft robots, wearable devices, and crossmodal perception robot systems based on multimodal sensor neural networks.

2. Results

2.1. Design and Fabrication of the e-Skin

In this study, an MM-based e-skin with multimodal fusion-sensing functions has been proposed. This system can simulate the auditory, visual, and tactile functions in the human nervous system and provide continuous real-time monitoring signals, as illustrated in **Figure 1a**. The e-skin was constructed using a multilayer structure, including a sensitive system and a substrate system, and its constituent parts are illustrated in Figure 1b.

The sensitive system consisted of an electret-piezoelectric composite film and a multiwalled carbon nanotube (MWNT) electrode. The composite film was fabricated by embedding the inorganic nanoparticles P(VDF-TrFE) and $BaTiO_3$ into the dielectric matrix of Ecoflex elastomers, followed by thermal charging. A schematic of the manufacturing process is provided in Supporting Information 1. A part of the $BaTiO_3$ content served as a nucleating agent for P(VDF-TrFE) to promote the formation of the piezoelectric-β phase, whereas the remainder of $BaTiO_3$ served as a piezoelectric phase. This composite film fulfilled two functions: sensing mechanical deformations (pressure and vibration) and identifying proximal distance. The upper surface of this dielec-

tric film was coated with MWNTs. When subjected to an external strain, the conductive network formed by the overlap of MWNTs underwent a local break, resulting in a change in resistance. The mechanical test results demonstrated that the sensitive system had good stretchability and could adapt to the deformation of dynamic skin. In addition, the modulus of elasticity of the electret layer was two orders of magnitude lower than that of the MM skeleton, and thus the e-skin could stretch freely without delamination.

To introduce biomimetic nonlinear mechanical properties into the e-skin, a substrate with a 4D printed mechanical metamaterial skeleton was designed, as illustrated in Figure 1c. The mechanical MM skeleton contained two representative topological arrangements (tetra/hexa-MMs) with horseshoe ligaments. Their auxetic and nonlinear mechanical behavior ensured high conformal deformation of the e-skin to dynamic tissue, allowing it to efficiently capture mechanical deformations in human motion, as illustrated in Figure 1d. Its applications were demonstrated using a wireless system and custom-made software. The system realized real-time exercise monitoring, speech recognition, near-field distance recognition, and playing somatosensory games. Figure 1e illustrates a schematic of the application scenarios.

2.2. Mechanical Model Skeleton

This section presents the derivation of the analytical solution for the normalized elastic modulus (E/E_s) and Poisson's ratio (v) of the four types of MMs undergoing uniaxial far-field stress. These MMs were divided into tetra- and hexa-MMs, according to the number of ligaments extending from the node. According to their geometrical configuration, the ligaments were divided into straight and horseshoe ligaments. A representative unit of an MM consisted of a rigid node and four or six ligaments distributed in a rotationally symmetrical manner. The influence of the key geometric parameters on the structural mechanical properties was investigated.

First, the Cartesian coordinate system $o'-x'y'$ was established, as illustrated in **Figure 2a,b**, and the central axis of the straight/horseshoe ligaments was described as a function of the arc length S as $X = X(S)$, $Y = Y(S)$. Each ligament was simplified as a simple supported ligament subjected to an axial force (N) and a shear force (Q) when subjected to external uniaxial stretching. The Euler-Bernoulli beam was used to simulate the deformation of the slender ligaments, and the nodes were assumed as rigid bodies. A schematic of the free-body diagram (FBD) and the key geometric parameters of the two types of units are illustrated in Figure 2c,d. Because of the rotational symmetry of the representative unit and the uniaxial uniform stress field, all external cut points in a unit cell were required to be moment- and force-free in the y-direction when they were in the *x*-direction stress field.

Here, γ represents the angle between the ligament and the connecting line, R is the radius of the tangential circle of the rigid node, L represents the length of the ligament, and D represents the distance between the center points of adjacent cells, w is the thickness of the ligament, $\_w$ is the normalized thickness of the ligament, η is the central angle of the arc ligament, and θ represents the angle between the ligament and the joined side of the
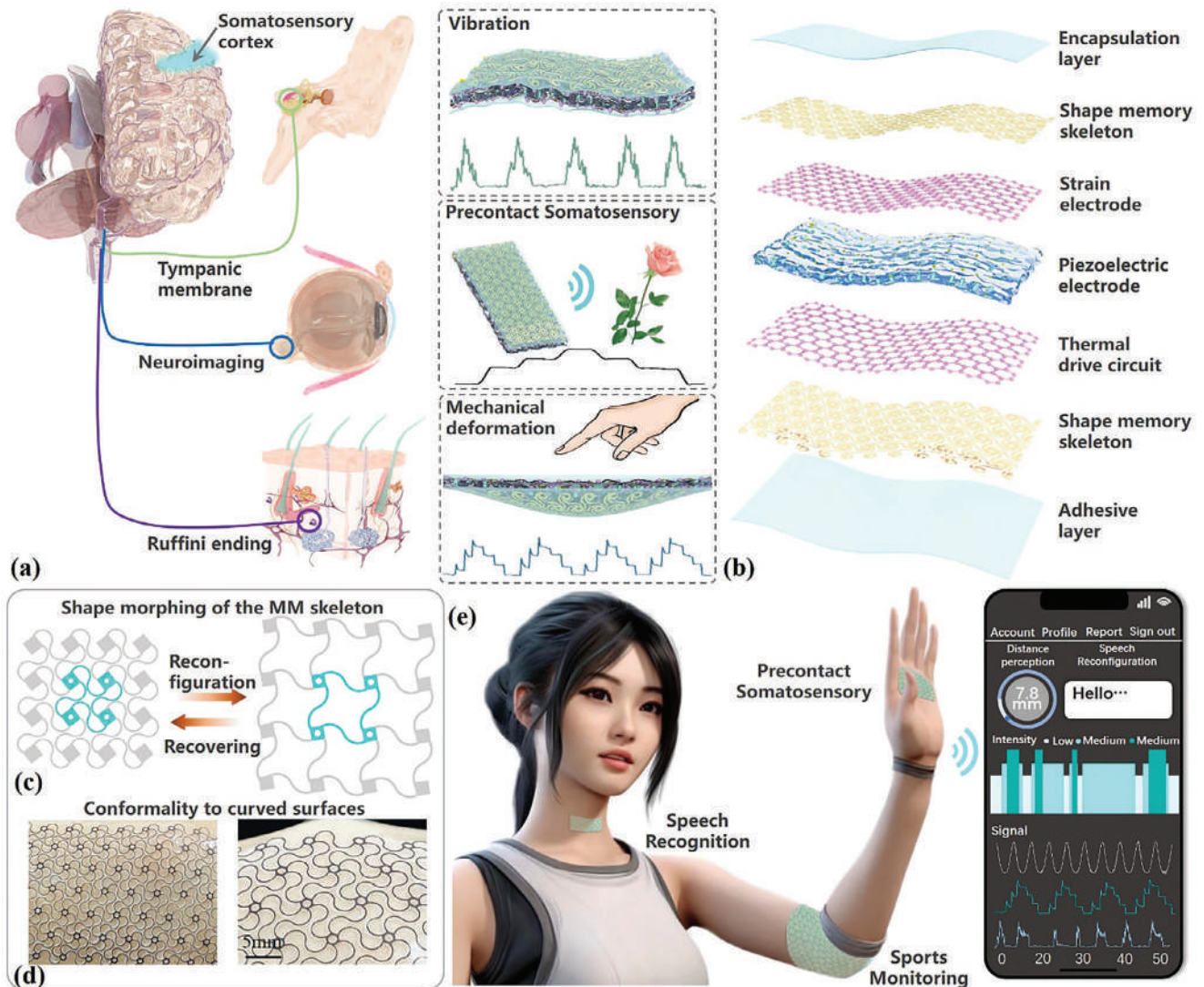
Figure 1. Schematic illustration of e-skin. a) Multimodal fusion perception nervous system and the corresponding three stimulation modes. b) Explored-view illustration of a multilayer device in the e-skin. c) Demonstration of the shape-morphing cycle of the MM skeleton: it is transformed into a new structure when an external force is applied and then heated to return to its pre-memorized shape. d) Conformal characteristics of e-skin when attached to spherical and saddle-shaped surfaces. e) Schematic illustrations of e-skin worn for sports monitoring, speech recognition, and near-field distance recognition.

rigid node. Figure 2e,f illustrates the configurations and geometric parameters of representative MM units. The other configurations used in this study are presented in Supporting Information 2. The total strain energy of a representative unit cell is

$$U = \frac{1}{2E_S A} \sum_{i=1}^{n} \int_0^{S_0} N^2 dS + \frac{1}{2E_S I} \sum_{i=1}^{n} \int_0^{S_0} M^2 dS \quad (1)$$

where S_0 denotes the total length of the ligament, n denotes the number of ligaments, E_s is the Young's modulus of the component materials, A denotes the cross-sectional area of the ligament, and I denotes the moment of inertia of the cross-section of the ligament(the cross-section of the ligament is assumed to be rectangular with uniform thickness, t, and unit depth, $I = w^3/12$).

For a tetra-MM with straight ligaments, the total strain energy of a unit is

$$U = 2\frac{(F\cos\gamma)^2 L}{2E_s A} + 2\frac{(P\cos\gamma)^2 L}{2E_s A} + 2\int_0^L \frac{(xP\sin\gamma)^2}{2E_s I} dx \quad (2)$$

The displacement of point 1 along the x-direction is obtained by

$$\delta_x = \partial U / \partial F|_{P=0} = \frac{FL}{E_s A}\cos^2\gamma + \frac{FL^3}{12E_s I}\sin^2\gamma \quad (3)$$

The strain in the x-direction is $\varepsilon_x = \sqrt{2}\delta_x/2D$. The total displacement of point 3 along the y-direction is derived according
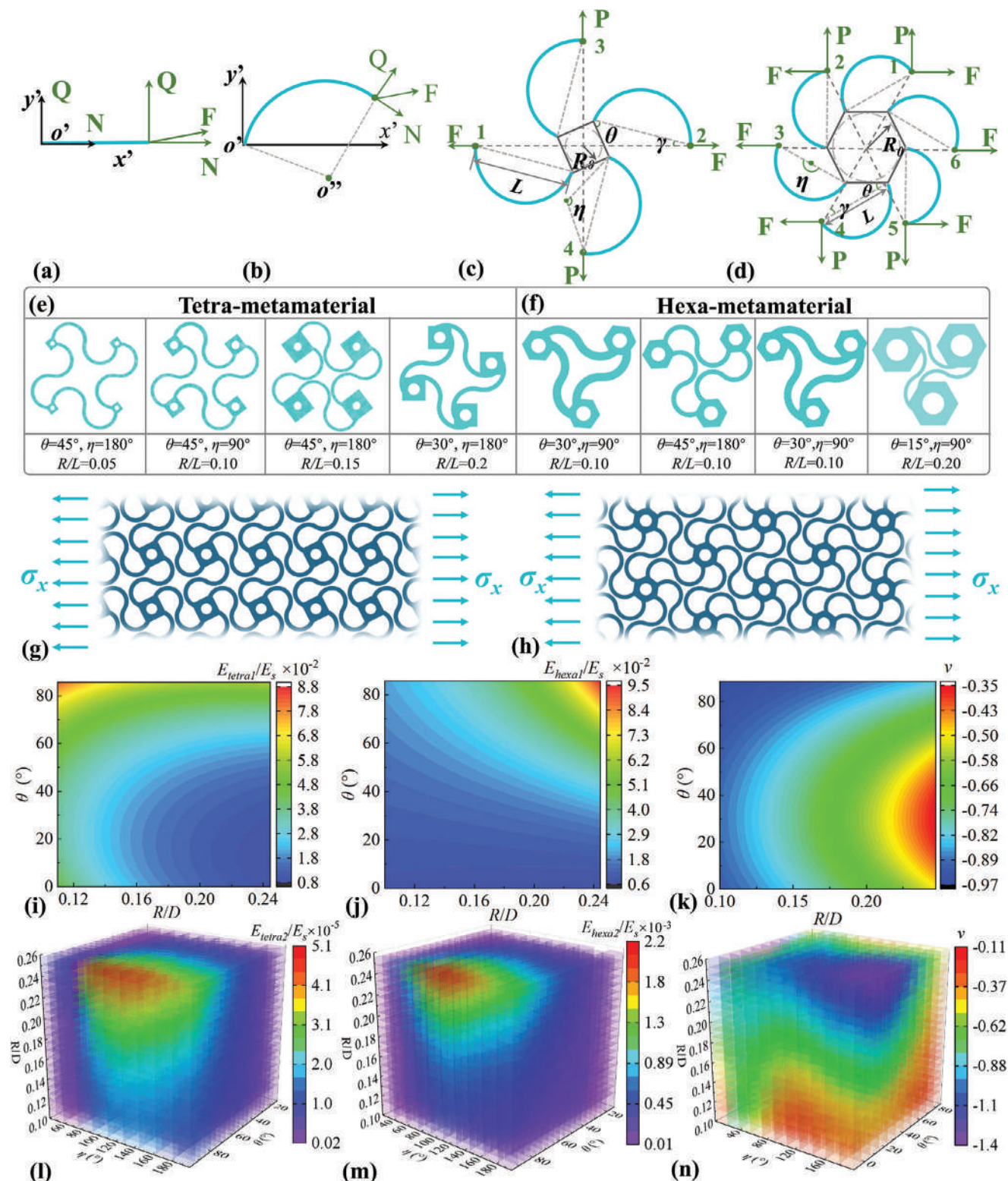
Figure 2. Mechanical model and theoretical results of the MMs: FBD of the a) straight and b) horseshoe ligaments. Mechanical model of a representative unit in c) tetra-horseshoe and d) hexa-horseshoe MMs. Geometric control parameters of the representative units in e) tetra-horseshoe and f) hexa-horseshoe MM skeletons, and g) tetra-horseshoe and h) hexa-horseshoe MMs under far-field uniaxial loads. Theoretical results of E/E_s of i) tetra- and j) hexa-MMs with straight ligaments. k) Theoretical results of ν for hexa-MMs with straight ligaments. Theoretical results of E/E_s of l) tetra- and m) hexa-MMs with horseshoe ligaments. n) Theoretical results of ν of hexa-MMs with horseshoe ligaments.

ADVANCED
SCIENCE NEWS

www.advancedsciencenews.com

ADVANCED
FUNCTIONAL
MATERIALS

www.afm-journal.de

to $\varepsilon_y = \partial U/\partial P|_{P=0} = 0$. The normalized elastic modulus of the metamaterials can be expressed as

$$E = \sigma_x/\varepsilon_x E_s \tag{4}$$

The Poisson's ratio is

$$\nu = -\varepsilon_y/\varepsilon_x \tag{5}$$

The normalized elastic modulus of the tetra-MM can be expressed as

$$E_{\text{tetra1}}/E_s = \sqrt{2}\bar{w}^3/\left(\bar{w}^2\cos^2\gamma + \sin^2\gamma\right) \tag{6}$$

According to the analytical theory, the Poisson's ratio of tetra-MMs with straight ligaments is always equal to 0, which results from the boundary conditions.

For a tetra-MM with horseshoe ligaments, the total strain energy in the ligament i is

$$U = \frac{L}{2E_sA} \sum_{i=1}^{4} \left(\beta_1 N_i^2 + \beta_2 N_i Q_i + \beta_3 Q_i^2\right)$$
$$+ \frac{L}{2E_sI} \sum_{i=1}^{4} \left[\beta_5(N_1L)^2 + \beta_6(Q_1L)^2 + \beta_9 N_1 Q_1 L^2\right] \tag{7}$$

The displacement of point 1 along the x-direction can be expressed as

$$\delta_x = \partial U/\partial F|_{P=0} = \frac{L}{E_sA} \left[\beta_1 F^2\cos^2\gamma + \beta_3 F^2\sin^2\gamma\right]$$
$$+ \frac{L^3}{E_sI} \left[\beta_5 F\cos^2\gamma + \beta_6 F\sin^2\gamma + \beta_9 F\sin\gamma\cos\gamma\right] \tag{8}$$

The normalized elastic modulus of the MM is

$$E_{\text{tetra2}}/E_s = \bar{w}^3/\left[\bar{w}^2\left(\beta_1\cos^2\gamma + \beta_3\sin^2\gamma\right) + 6\left(\beta_5\cos^2\gamma + \beta_6\sin^2\gamma + \beta_9\sin\gamma\cos\gamma\right)\right] \tag{9}$$

and its Poisson's ratio is $\nu_{\text{tetra2}} = -\varepsilon_y/\varepsilon_x = 0$.

Using the same methods as in the previous section, the normalized elastic modulus (E_{hexa1}, E_{hexa2}) and the Poisson's ratio (ν_{hexa1}, ν_{hexa2}) of the hexa- and horseshoe hexa-MMs were derived (details can be found in Supporting Information 4).

$$E_{\text{hexa1}}/E_s = 2\sqrt{3}\bar{w}^3/\varphi_2 \tag{10}$$

$$\nu_{\text{hexa1}} = -\sqrt{3}\varphi_6/\varphi_2 \tag{11}$$

$$E_{\text{hexa2}}/E_s = \bar{w}^3/\left(6\beta_5\varphi_1 + 6\beta_6\varphi_2 + 3\beta_9\varphi_3\right) \tag{12}$$

$$\nu_{\text{hexa2}} = -\sqrt{3}\left[\beta_9\varphi_4 + \left(\beta_5 - \beta_6\right)\varphi_5\right]/\left(2\beta_5\varphi_1 + 2\beta_6\varphi_2 + \beta_9\varphi_3\right) \tag{13}$$

The geometric configuration of hexa- and tetra-units are determined by R/D and θ, and their mapping relations with γ and L are presented in Figure S6g,h (Supporting Information). η determines the degree of bending of the horseshoe ligaments. The contour plots in Figure 2i–k illustrates the theoretical results of the impact of the geometrical parameters on E/E_s and

ν under infinitesimal deformation for MMs with straight ligaments. θ was varied from 0° to 90°, the normalized width R/D varied from 0.1 to 0.3, and the normalized thickness _w was fixed at 0.05.

It can be observed that for tetra-MMs, E_{tetra1}/E_s decreases monotonically with increasing R/D. As θ increases from 0 to 90°, E_{tetra1}/Es first decreases and then increases. For hexa-MMs, E/E_s increase monotonously with increasing R/D and θ. These geometric parameters also influence the Poisson's ratio. For hexa-MMs with straight ligaments, the Poisson's ratio exhibits a tunable domain from -0.35 to ≈-0.97. As illustrated in Figure 2k, the auxetic effect decreases monotonically with increasing R/D. As θ increases from 0° to 90°, ν first increases and then decreases.

For the mechanical MMs with horseshoe ligaments, their mechanical properties were mainly affected by R/D, θ, and η. The central angle of the horseshoe ligaments (η) varied from 0° to 180°. All equivalent moduli were reduced by one to three orders of magnitude compared to the MMs with straight ligaments. The analytical results are illustrated with highlights of the effects of θ, R/D, and η in Figure 2l–n. From these results, it can be observed that the variation range of ν is expanded to (−0.11 ≈−1.4). This indicates that by changing the geometric configuration of the ligaments, the auxetic properties of MMs can be greatly improved. Furthermore, the mechanical performance of MMs can be adjusted by changing their topological arrangements and key geometric parameters.

2.3. Nonlinear and Reconfigurable Mechanical Behavior

MMs can usually sustain considerably larger uniaxial tensile strains than their constituent materials owing to their artificial structure and topological arrangements. The stretchability of MMs with straight ligaments depends mainly on the rotation of the structural nodes. However, the wavy ligaments of the horseshoe MMs significantly increase their stretchability by inducing a bending-dominated phase in the structural deformation pattern. In this section, the mechanical behavior of MMs with straight and horseshoe ligaments under large deformations has been comparatively studied.

Uniaxial tensile experiments and finite element analysis (FEA) were carried out to investigate the effect of the geometric parameters, including R/L, θ, and η, on the MMs. The commercial software ABAQUS (3DS Dassault Systemes, France) was used to analyze the mechanical behavior of the MMs. The central areas in sufficiently large models (11 × 6 unit cells) were utilized to avoid possible edge effects. C3D8 solid units and static analysis steps were adopted, the film and MM skeleton were bound by tie constraints, and the central reference points 1 and 2 were set at both ends of the component. Reference point 1 was set as a fixed support condition to constrain all degrees of freedom and displacement boundary conditions were set for reference point 2 to simulate the mechanical behavior of tension and compression. The evaluation of ν was derived from the original configurations $\nu = \varepsilon_x/\varepsilon_y$ and $\lambda = \Delta\varepsilon_y/\varepsilon_y$, where ε_x and ε_y are the transverse and applied strains, respectively. The MMs as well as horseshoe-MMs exhibited auxetic effects (see details in Video S1, Supporting Information). The MMs provided a wide range of negative Poisson's ratios (from 0 to -1.08) with a
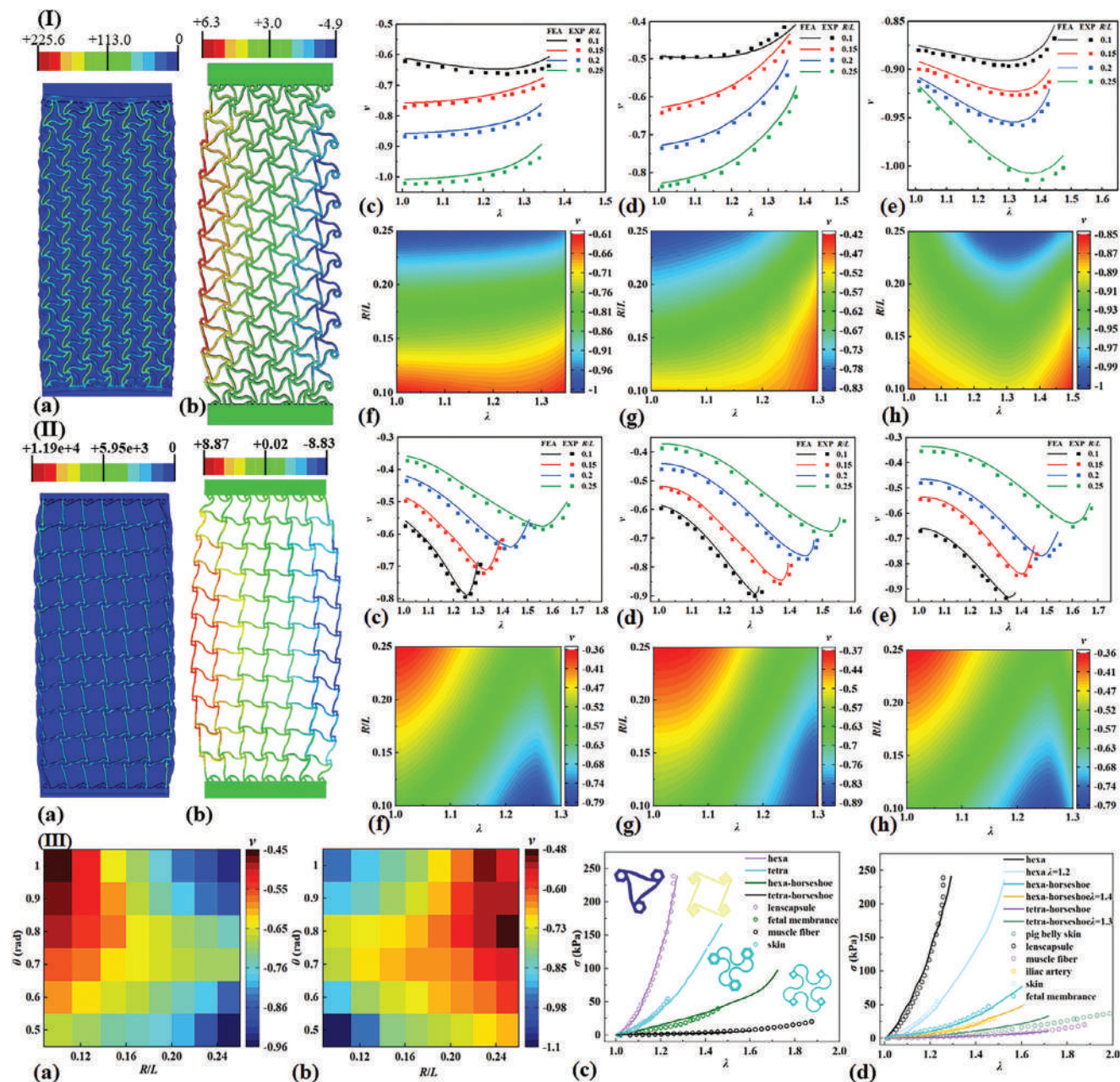
Figure 3. Mechanical properties and reverse design strategy of the MM skeleton: (I-a) Stress contour diagram of a hexa-MM substrate under uniaxial tension, b) transverse strain contour diagram of a hexa-MM skeleton subjected to uniaxial tensile loads; v–λ curves and contour plots of hexa-MMs with $\theta =$ (c) and (f) 30°, (d) and (g) 45°, and (e) and (h) 60°. (II-a) Stress contour diagram of a tetra-MM substrate under uniaxial tension, b) transverse strain contour diagram of a tetra-MM skeleton subjected to uniaxial tensile loads, v-λ curves and contour plots of tetra-metamaterials with $\theta =$ (c) and (f) 30°, (d) and (g) 45°, and (e) and (h) 60°. III) Heatmap of the Poisson's ratio as a function of R/L and θ for a) tetra and b) hexa units. c) Comparison of σ−λ curves between metamaterials and tissues/organs.[45] d) Shape memory conversion between biological tissues through programming.

large strain range (up to 71%). The mechanical properties could be adjusted by changing either of the crucial parameters (η, θ, and R/L). For the straight ligament MMs, the auxeticity performance results from the rotation of structure nodes, and v ranged from 0 to -0.7. Compared to the straight ligaments (Figures S7 and S8, Supporting Information 5), the structures with horseshoe ligaments nearly doubled the range of v, as illustrated in **Figure** 3I,II.

For hexa-MMs, the transverse strain, λ_{tr}, increased as θ increased and decreased as R/D increased, whereas v_{min} decreased as θ increased and increased as R/D increased. For tetra-MMs, the λ_{tr} increased as R/L increased and decreased as R/D increased, whereas v_{min} decreased as θ decreased and increased as R/D increased. These results indicate that the key parameters (R/D, θ, and η) could be utilized to adjust the mechanical properties of the MMs. The turntable domain of v along the horizontal

direction is −1.08 to 0.05. Furthermore, the average elongation with horseshoe ligaments increased by ≈17–22% for MMs with the same topological pattern and geometric parameters.

Therefore, it can be inferred that horseshoe ligaments significantly enhance the stretchability, auxetic properties, and flexibility of MMs. The responses of the MM skeletons and the assembled MM e-skin to uniaxial tensile loads were determined using FEA. It can be intuitively observed from Figure S9 (Supporting Information) that the MMs and horseshoe ligaments significantly enhance the auxetic effect of the e-skin when subjected to uniaxial tensile loads. The enlargement of adjusting the Poisson's ranges mainly results from the bending of the ligaments and the enhanced rotation of the lattice nodes. Furthermore, when subjected to large strains, horseshoe MMs exhibit different configurations compared to straight-ligament materials and exhibit superior auxetic performance. For horseshoe MMs, the deformation is dominated by the bending of the ligaments in the initial stage, where ν has a stable value as λ increases. As the relative strain exceeds the transverse value (λ_{tr}), ν reaches the minimum value (ν_{min}) and then increases sharply to zero. The heat maps in Figure 3IIIa,b demonstrate the relationship between the geometric configuration of metamaterial units and the minimum negative Poisson's ratio.

Due to the abundant design space, the designed MMs can imitate the nonlinear mechanical behavior of specific biological tissues[45] as shown in Figure 3III-c. Furthermore, benefiting from its electrically driven shape memory reconstruction function, the biomimetic nonlinear mechanical properties of metamaterials can be transformed between different biological tissues, as shown in Figure 3III-d and Figure S5 (Supporting Information). For example, the nonlinear σ-λ response of hexa-MMs before and after reconstruction was similar to that of lens capsule and skin, respectively.

2.4. Output Characteristics of the e-Skin

In this section, the multimodal sensing performance of the MM e-skin is described. First, the precontact electrical output performance of the e-skin was evaluated. Electrets with different surface charge densities were obtained by applying the same thermal charge treatment to the piezoelectric films with different particle contents. The electrical signal of the electric receptor on the proximal target was simulated using the commercial software COMSOL, as illustrated in **Figure 4a**. Subsequently, their perception of the same target (polytetrafluoroethylene (PTFE) film) at a distance of 5–60 mm was tested, as illustrated in Figure 4b and Video S2 (Supporting Information). It can be seen that the sensitivity and output voltage increase with increasing surface charge density, which is consistent with the results of the simulation (see Supporting Information 6 and Figure S10, Supporting Information). Further, the sensitivity of the device to distance recognition was demonstrated, as illustrated in Figure 4c, showing its application value in proximal sensing.

Subsequently, the piezoelectric properties of the e-skin were characterized. The output signals of the gradient pressure and gradient frequency load were obtained as illustrated in Figure 4d. An evenly distributed load with a fixed frequency (1 Hz) and pressure (1 kPa) was applied to the e-skin, and a short-circuit current

output result was obtained. The average open-circuit voltage (V_{oc}) of the different e-skins under an external load was characterized, as illustrated in Figure 4e. The V_{oc} of the e-skin was found to increase with increasing volume fraction of the particles in the film under the same pressure. The output signal also exhibited good linearity with increasing pressure.

Finally, the response of the e-skin to in-plane strain was evaluated. The electrical reliability of the e-skin with representative MM skeletons was characterized through loading–unloading experiments, as illustrated in Figure 4f. The test results confirmed that the configuration of the MM skeleton significantly affected the strain sensitivity of the e-skin. E-skins with different MM skeletons produced different electrical signal feedbacks to the same input signal because the MMs influenced the dispersion of the conductive network. The relative resistance values could be restored to the original state in each cycle, indicating that the conductive network possessed good repairability. This excellent stability and repeatability mainly resulted from the high-density conductive network formed by the deposition of carbon-based materials on the sensor surface and its tight bonding to the Ecoflex substrates. The Gauge factor (GF) and linearity (R^2) of the e-skin to the in-plane strain were obtained from the uniaxial tensile test. GF is commonly utilized to evaluate the sensitivity of sensors and can be obtained by the relative change in resistance ($\Delta R/R_0$) to the applied strain (λ). The larger the GF, the higher the sensitivity. It can be expressed as:

$$\text{GF} = \frac{\Delta R}{\lambda R_0} \tag{14}$$

where ΔR represents a numerical change in resistance, R_0 represents the initial values of resistance, and λ represents the strain of the sensor.

$$R^2 = \sum \frac{(\text{explained variation})^2}{(\text{total variation})^2} \tag{15}$$

Figure 4g displays the GF–λ curves of the e-skin with different skeletons. The three curves demonstrated an overall bending upward trend in the 0–20% region, and the resistance changed slowly when the strain was small. In contrast, devices without MM structures exhibited relatively small changes in resistance when subjected to the same external tensile load. This implies that the sensitivity of the sensors with an MM skeleton is considerably higher than that of the sensors without it, reflecting the advantage of sensitivity enhancement. The linearity and GF results are presented in Table S5, Supporting Information (Supporting Information 6). It is worth noting that the geometric design of the horseshoe ligaments further improves the sensitivity attributed to the enhancement in the degree of separation of the sensitive materials under tensile strain, as illustrated in Figure 4h. The mechanism of strain sensing involves altering the conductive path through the deformation of conductor materials, resulting in a change in material resistance. For a structure with a positive Poisson's ratio, applying tensile strain in the x-direction causes contraction in the y-direction. This leads to increased dispersion of the conductive material in the x-direction but decreased dispersion in the y-direction. Such an offsetting effect limits the sensitivity of the strain sensor. In this study, mechanical metamaterials
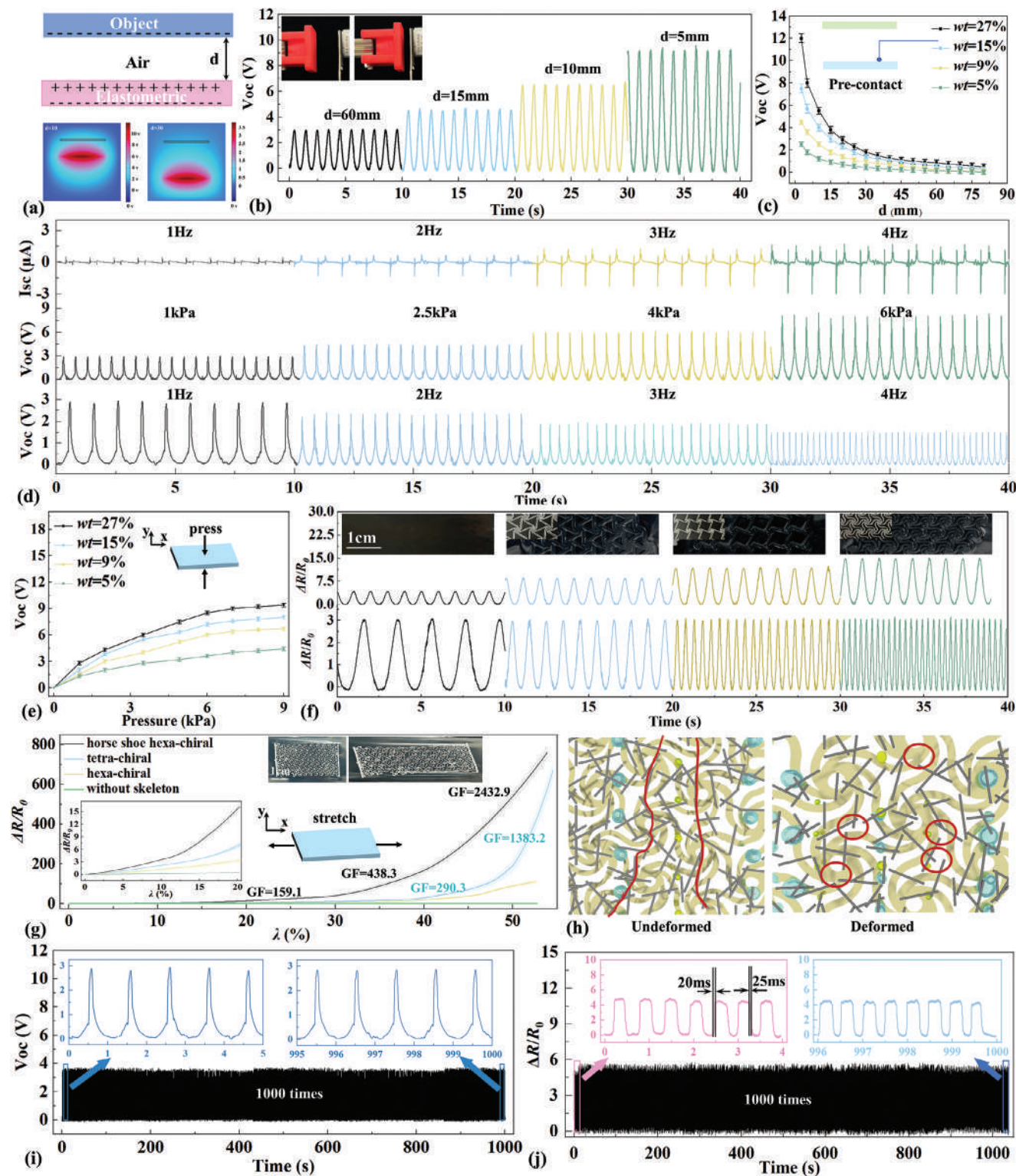
Figure 4. Characteristics of e-skin for multimodal sensing. a) Simplified physical model of the electroreceptor and its simulated outputs when a PLA approaches with gradient distance, b) response of a precontact sensor to the single axis sinusoidal motion of the object with gradient distance, c) electrical response of the precontact, d) output current results when subjected to uniform sinusoidal pressure loads, e) relationship between the output voltage and the uniform pressure loads of the e-skin, f) optical images of the MM e-skin and the response characterization results of the e-skin obtained through the loading-unloading cycle tests under gradient tensile strain and tensile speeds, g) comparison of the sensitivity of the e-skin under uniaxial tensile loads corresponding to the three types of MM skeletons, h) schematic of the changes in the conductive pathway before and after deformation, and durability test of the e-skin under i) uniform pressure load and j) uniaxial tensile loads.

ADVANCED
SCIENCE NEWS
www.advancedsciencenews.com

ADVANCED
FUNCTIONAL
MATERIALS
www.afm-journal.de

were integrated into the e-skin structure, endowing it with a negative Poisson's ratio characteristic. This improvement enhanced the dispersion of conductive particles on the surface of the e-skin when subjected to tensile load, thereby significantly increasing its sensitivity to strain. The GF of the e-skin with a horseshoe ligament MM increased to 2432.85, which is approximately 20 times that of the e-skin with a straight ligament MM. In addition, a durability test of the piezoelectric e-skin was conducted over 1000 cycles. The test results of 0–5 and 996–1000 repetitions were compared, as shown in Figure 4i, which indicates its superior stability. Subsequently, a dynamic tensile cyclic loading experiment demonstrated its superior durability and extremely short response time (≈20 ms) to pressure, as shown in Figure 4j.

2.5. Multimodal Sensing of the e-Skin

The proposed self-powered e-skin can obtain energy from the environment or users' action without relying on external power sources. Furthermore, by integrating with a microcontroller, this e-skin achieved continuous self-powered monitoring and wireless signal transmission. Compared to traditional electronic devices, this self-powered e-skin achieves long-term usability, convenience, and lightweight. This section demonstrated the multimodal sensing function of the self-powered e-skin by real-time wireless information transmission and human-machine interaction functions for multiple scenes and senses, as illustrated in **Figure 5a**. The customized wireless data transmission and data visualization systems are illustrated in Supporting Information 7. By the detection and recognition of sound signals, real-time monitoring of human movement, near-field target positioning, somatosensory games, and other real-scene functions, it was confirmed that the sensor could be applied to a variety of real scenarios.

To verify its ability to monitor the motion signals of the joints, we pasted the sensor on a finger knuckle, wrist, elbow, and knee, as illustrated in Figure 5b. First, the e-skin was attached to the second knuckle of the index finger for testing. The finger joint was continuously bent inward by 0°, 30°, 60°, and 90°, and each bending angle was kept stable for a few seconds and then restored from 90° to 0° as a complete test cycle. Each cycle was repeated four times. Although there is some jitter in the curves, which might be due to the shaking of the finger and the speed of bending, all the e-skins can distinguish the gradient bending angles of the finger joints through the peak characteristics of the signal. Motion tests in the wrist, knee, and elbow were performed using the same test methods (see real-time monitoring video in Video S3, Supporting Information).

Pronunciation-syllable detection and motion tests were also performed. Syllable detection by the sensor was performed using an audio source. Three commonly used words, "hi," "happy," and "population," with different syllables were selected, corresponding to monosyllables, two-syllables, and four-syllables. As illustrated in Figure 5c, the sensor was covered with a Bluetooth speaker to detect tiny vibrations of the speaker. Each word was composed of several syllables, each of which corresponds to a small vibration related to the spikes on the curve. The number of syllables and resistance response spikes correspond to each other,

indicating that the four words could be successfully detected. The sensor responded remarkably even though the relative resistance changes were very small, demonstrating that it could detect extremely small vibrations.

The sensitivity of the precontact sensing function is affected by the charge density of the object to be measured and the sensor surface, and it is possible to achieve precise sensing of the relative distances for specific objects and devices. Based on the aforementioned principles and the stable output of the sensing signal, as illustrated in Figure 5d, we developed a real-time near-field distance-sensing interface using the LabVIEW program. When a naturally charged target approaches, the output voltage of the e-skin is monitored and converted into a distance signal in real time. The signal was wirelessly transmitted to a data acquisition board via Wi-Fi and converted into a distance signal output. The flexible human–computer human–machine interaction function could also be used to immersively control virtual game characters, as shown in Figure 5e. In this study, the noncontact control pad was used to control the famous computer game "Angry Birds." In this system, we used the distance between the hand and the control panel to control the flying height of the bird to avoid obstacles. A demonstration of users playing the Angry Birds game through contactless interaction is shown in Figure 5f and Video S4 (Supporting Information).

3. Conclusion

In this study, we have proposed a MM-based self-powered e-skin with a multimodal fusion perception function that realizes real-time acquisition of hearing, touch, and visual multimodal signals. First, by imitating the mechanical properties of bio-tissues, we designed a series of MMs and developed theoretical models to obtain analytical solutions for their Poisson's ratio and elastic modulus. Subsequently, the influence of the topological parameters on the mechanical properties of the MMs was verified through experimental and finite element analyses. Further, reconfigurable mechanical properties of MMs were clarified through transformation between different bio-tissues.

Assembling a mechanical MM in the layered e-skin not only improved the mechanical disorders between the e-skin and human tissues but also improved the sensitivity and linearity of the strain sensor. It is worth noting that the value of GF of the e-skin with the horseshoe ligament MM increased to 2432.85 with a linearity above 0.98, which is approximately 20 times that of the e-skin with the straight ligament MM. The measurable strain range was increased to 50% for the MM e-skin with a short response time of 20 ms. The e-skin exhibited a sensitivity of 3 kPa^{-1} and could maintain consistent performance over 10 000 cycles. In addition, inspired by bioinductive systems, we have achieved tactile perception and precontact visual perception functions by integrating self-powered artificial receptors on the e-skin. It can not only perceive and recognize tactile signals but also achieve visual perception through a stable voltage output based on the distance and charges carried by the approaching target. Finally, the multimodal signal acquisition function of the self-powered e-skin was verified by the real-time detection of human motion information, sound signal recognition, and somatosensory games. The self-powered e-skin converts widely available mechanical energy into electrical energy needed for information perception. This
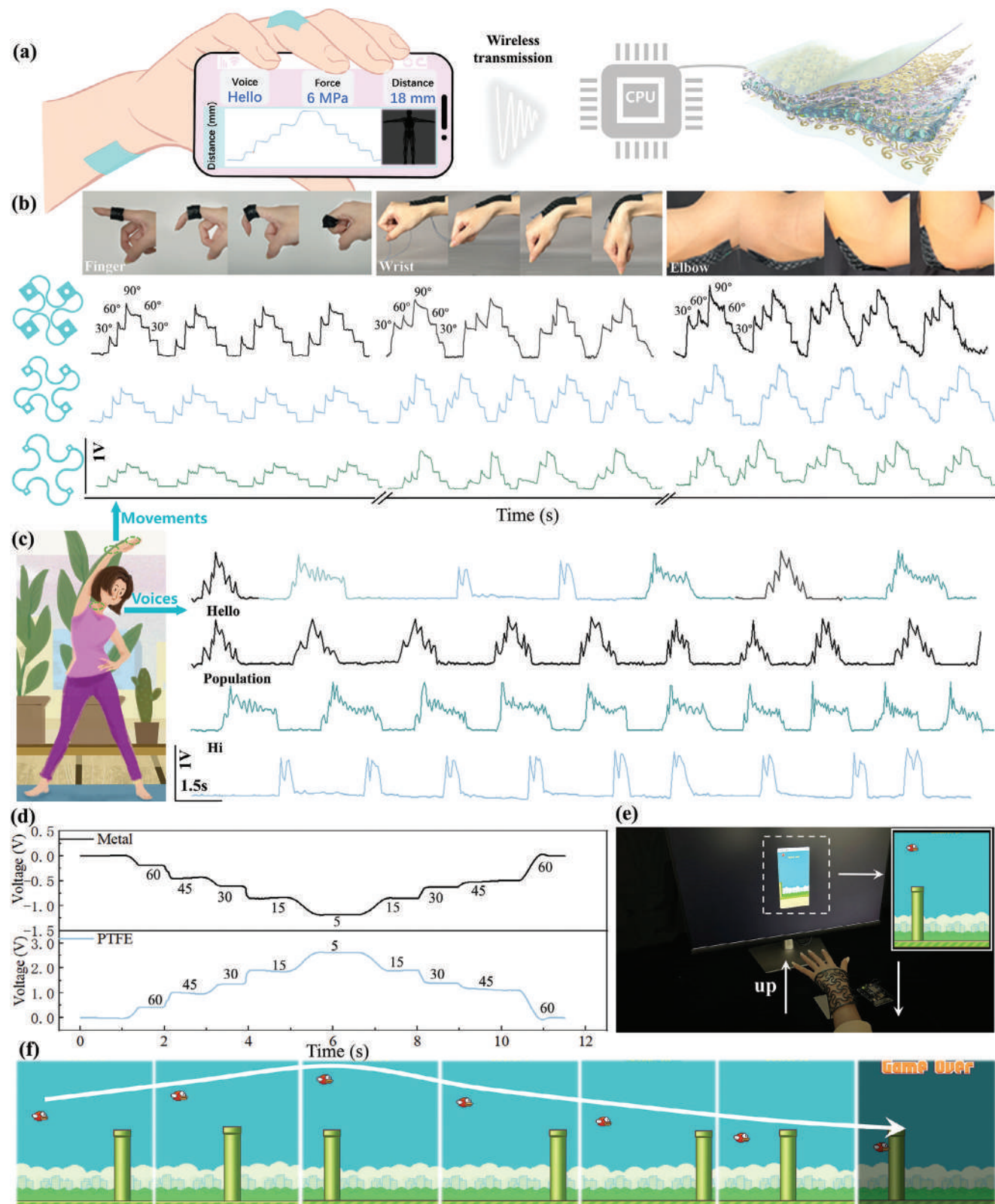
Figure 5. a) Integration of the wireless monitoring system based on the MM e-skin. b) Real-time motion monitoring of a finger, wrist, and elbow at different bending angles with different MM e-skins. c) Real-time acoustic monitoring results for different words. d) Real-time output response of the e-skin to the proximity of the external targets. e) Playing somatosensory games using the near-field distance recognition function of the e-skin. f) Schematic for controlling the flight altitude of a game mission using the noncontact distance perception function of the e-skin.

**ADVANCED
SCIENCE NEWS**

www.advancedsciencenews.com

**ADVANCED
FUNCTIONAL
MATERIALS**

www.afm-journal.de

strategy eliminates the dependence of wearable electronic devices on external power sources, reduces the weight of wearable devices, and achieves passive and wireless sensing functions in e-skin.

In brief, an artificial e-skin not only realizes excellent reconfigurable mechanical properties similar to the biological skin but also integrates the self-powered multimodal signal acquisition functions. It is expected to apply to crossmodal perception robot systems based on multisensory neural networks.

4. Experimental Section

The fabrication process of the e-skin is described in Supporting Information 1. The details of the design strategies for metamaterial skeletons are summarized in Supporting Information 2. The thermal-driven process of the shape memory e-skin is illustrated in Supporting Information 3. The derivation process of the analytical model is illustrated in Supporting Information 4. The effects of geometrical parameters on the non-linear mechanical properties and the reversal design strategy are analyzed in Supporting Information 5. Finally, details of the electrical experiments and characteristics of e-skin are provided in Supporting Information 6. The customized wireless data transmission system is illustrated in Supporting Information 7.

Supporting Information

Supporting Information is available from the Wiley Online Library or from the author.

Conflict of Interest

The authors declare no conflict of interest.

Data Availability Statement

The data that support the findings of this study are available from the corresponding author upon reasonable request.

[1] X. Wan, Z. M. Xiao, Y. J. Tian, M. Chen, F. Liu, D. Wang, Y. Liu, P. J. D. Bartolo, C. Z. Yan, Y. S. Shi, R. R. Zhao, H. J. Qi, K. Zhou, *Adv. Mater.* **2024**, 2312263.

[2] M. Koo, K. I. Park, S. H. Lee, M. Suh, D. Y. Jeon, J. W. Choi, K. Kang, K. J. Lee, *Nano Lett.* **2012**, *12*, 4810.

[3] N. Li, W. Zhao, F. F. Li, L. W. Liu, Y. J. Liu, J. S. Leng, *Matter* **2023**, *6*, 940.

[4] S. D. Luo, T. Liu, *Adv. Mater.* **2013**, *25*, 5650.

[5] H. Zhang, N. S. Liu, Y. L. Shi, W. J. Liu, Y. Yue, S. L. Wang, Y. N. Ma, L. Wen, L. Y. Li, F. Long, Z. G. Zou, Y. H. Gao, *ACS Appl. Mater. Interfaces* **2016**, *8*, 22374.

[6] G. Lanzara, N. Salowitz, Z. Q. Guo, F. K. Chang, *Adv. Mater.* **2010**, *22*, 4643.

[7] I. You, D. G. Mackanic, N. Matsuhisa, J. Kang, J. Kwon, L. Beker, J. Mun, W. Suh, T. Y. Kim, J. B. H. Tok, Z. N. Bao, U. Jeong, *Science* **2020**, *370*, 961.

[8] A. Chortos, J. Lim, J. W. F. To, M. Vosgueritchian, T. J. Dusseault, T. H. Kim, S. Hwang, Z. N. Bao, *Adv. Mater.* **2014**, *26*, 4253.

[9] Z. H. Guo, H. L. Wang, J. J. Shao, Y. S. Shao, L. Y. Jia, L. W. Li, X. Pu, Z. L. Wang, *Sci. Adv.* **2022**, *8*, eabo5201.

[10] C. Ye, C. Ume, S. Sitaraman, *J. Electron. Packag.* **2020**, *142*, 021007.

[11] C. M. Boutry, M. Negre, M. Jorda, O. Vardoulis, A. Chortos, O. Khatib, Z. N. Bao, *Sci. Rob.* **2018**, *3*, eaau6914.

[12] Z. Y. Xiang, L. H. Li, Z. H. Lu, X. X. Yu, Y. W. Cao, M. Tahir, Z. Y. Yao, Y. L. Song, *Matter* **2023**, *6*, 554.

[13] D. Y. Khang, H. Jiang, Y. Huang, J. A. Rogers, *Science* **2006**, *311*, 208.

[14] X. Huang, W. Guo, S. Liu, Y. Li, Y. Qiu, H. Fang, G. Yang, K. Zhu, Z. Yin, Z. Li, H. Wu, *Adv. Funct. Mater.* **2022**, *32*, 2109109.

[15] Y. Xu, W. Guo, S. Zhou, H. Yi, G. Yang, S. Mei, K. Zhu, H. Wu, Z. Li, *Adv. Funct. Mater.* **2022**, *32*, 2200961.

[16] S. Jiang, X. J. Liu, J. P. Liu, D. Ye, Y. Q. Duan, K. Li, Z. P. Yin, Y. A. Huang, *Adv. Mater.* **2022**, *34*, 2200070.

[17] M. Amjadi, M. Turan, C. P. Clementson, M. Sitti, *ACS Appl. Mater. Interfaces* **2016**, *8*, 5618.

[18] W. J. Song, Y. Lee, Y. Jung, Y. W. Kang, J. Kim, J. M. Park, Y. L. Park, H. Y. Kim, J. Y. Sun, *Sci. Adv.* **2021**, *7*, eabg9203.

[19] F. Y. Liao, Z. Zhou, B. J. Kim, J. W. Chen, J. L. Wang, T. Q. Wan, Y. Zhou, A. T. Hoang, C. Wang, J. F. Kang, J. H. Ahn, Y. Chai, *Nat. Electron.* **2022**, *5*, 84.

[20] C. Zhang, H. Dong, C. Zhang, Y. Fan, J. Yao, Y. S. Zhao, *Sci. Adv.* **2021**, *7*, eabh3530.

[21] H. C. Zhao, K. O. Brien, S. Li, R. F. Shepherd, *Sci. Rob.* **2016**, *1*, eaai7529.

[22] T. T. Liu, Y. H. Zhu, J. C. Shu, M. Zhang, M. S. Cao, *Mater. Today Phys.* **2023**, *31*, 100988.

[23] D. Mandal, S. Banerjee, *Sensors* **2022**, *22*, 820.

[24] P. Xue, C. Valenzuela, S. S. Ma, X. Zhang, J. Z. Ma, Y. H. Chen, X. H. Xu, L. Wang, *Adv. Funct. Mater.* **2023**, *33*, 2214867.

[25] M. Segev-Bar, H. Haick, *ACS Nano* **2013**, *7*, 8366.

[26] X. L. Wang, H. Hu, Y. D. Shen, X. C. Zhou, Z. J. Zheng, *Adv. Mater.* **2011**, *23*, 3090.

[27] S. Yun, X. F. Niu, Z. B. Yu, W. L. Hu, P. Brochu, Q. B. Pei, *Adv. Mater.* **2012**, *24*, 1321.

[28] N. S. Lu, C. Lu, S. X. Yang, J. Rogers, *Adv. Funct. Mater.* **2012**, *22*, 4044.

[29] L. Shi, Z. Li, M. Chen, Y. Qin, Y. Jiang, L. Wu, *Nat. Commun.* **2020**, *11*, 3529.

[30] S. Yang, Y. He, J. S. Leng, *Int. J. Smart Nano Mater.* **2022**, *13*, 1.

[31] W. Zhao, J. Zhu, L. W. Liu, Y. J. Liu, J. S. Leng, *Int. J. Smart Nano Mater.* **2023**, *14*, 1.

[32] J. S. Wang, G. Wang, X. Q. Feng, T. Kitamura, Y. L. Kang, S. W. Yu, Q. H. Qin, *Sci. Rep.* **2013**, *3*, 03102.

[33] Z. L. Zhao, H. P. Zhao, J. S. Wang, Z. Zhang, X. Q. Feng, *J. Mech. Phys. Solids* **2014**, *71*, 64.

[34] R. Lakes, T. Lee, A. Bersie, Y. C. Wang, *Nature* **2001**, *410*, 565.

[35] D. H. Kim, N. S. Lu, R. Ma, Y. S. Kim, R. H. Kim, S. D. Wang, J. Wu, S. M. Won, H. Tao, A. Islam, K. J. Yu, T. I. Kim, R. Chowdhury, M. Ying, L. Z. Xu, M. Li, H. J. Chung, H. Keum, M. McCormick, P. Liu,

**ADVANCED
SCIENCE NEWS**

www.advancedsciencenews.com

**ADVANCED
FUNCTIONAL
MATERIALS**

www.afm-journal.de

Y. W. Zhang, F. G. Omenetto, Y. G. Huang, T. Coleman, J. A. Rogers, *Science* **2011**, *333*, 838.

[36] G. Lanzara, N. Salowitz, Z. Guo, F. K. Chang, *Adv. Mater.* **2010**, *22*, 4643.

[37] Y. Li, N. Li, W. Liu, A. Prominski, S. H. Kang, Y. H. Dai, Y. D. Liu, H. W. Hu, S. Wai, S. L. Dai, Z. Cheng, Q. Su, P. Cheng, C. Wei, L. H. Jin, J. A. Hubbell, B. Z. Tian, S. H. Wang, *Nat. Commun.* **2023**, *14*, 4488.

[38] W. C. Kyoung, H. S. Sung, J. H. Yongseok, H. K. Ja, H. K. Jeong, B. Seungmin, H. Taeghwan, H. K. Dae, *Chem. Rev.* **2022**, *122*, 5068.

[39] H. D. Espinosa, A. L. Juster, F. J. Latourte, O. Y. Loh, D. Gregoire, P. D. Zavattieri, *Nat. Commun.* **2011**, *2*, 173.

[40] Q. Ma, Y. Zhang, *J. Appl. Mech.-Trans. ASME* **2016**, *83*, 111008.

[41] W. Yang, V. R. Sherman, B. Gludovatz, E. Schaible, P. Stewart, R. O. Ritchie, M. A. Meyers, *Nat. Commun.* **2015**, *6*, 6649.

[42] K. I. Jang, H. U. Chung, S. Xu, C. H. Lee, H. Luan, J. Jeong, H. Cheng, G. T. Kim, S. Y. Han, J. W. Lee, J. Kim, M. Cho, F. Miao, Y. Yang, H. N. Jung, M. Flavin, H. Liu, G. W. Kong, K. J. Yu, S. I. Rhee, J. Chung, B. Kim, J. W. Kwak, M. H. Yun, J. Y. Kim, Y. M. Song, U. Paik, Y. Zhang, Y. Huang, J. A. Rogers, *Nat. Commun.* **2015**, *6*, 6566.

[43] Y. Jiang, Z. Liu, N. Matsuhisa, D. Qi, W. R. Leow, H. Yang, J. Yu, G. Chen, Y. Liu, C. Wan, Z. Liu, X. Chen, *Adv. Mater.* **2018**, *30*, 1706589.

[44] C. Zhang, H. Dong, C. Zhang, Y. Fan, J. Yao, Y. S. Zhao, *Sci. Adv.* **2021**, *7*, eabh3530.

[45] S. S. Sheiko, A. V. Dobrynin, *Macromolecules* **2019**, *52*, 7531.